PAPER

Check for updates

Urea-functionalized HKUST-1 metal–organic framework for high-performance lead adsorption

Nada M. Hashad,[a] Mostafa Y. Nassar, [ID] *[b] Hossam S. Jahin,[cd] Ahmed M. El-Nahas, [ID] [a] Mohamed S. S. Adam, [ID] [b] Elbadawy A. Kamoun,[b] Ibrahim Alfurayj,[b] Mohammed S. Ayoup,[b] Safinaz H. El-Demerdash[a] and Ahmed S. Abou-Elyazed [ID] *[ae]

Heavy metal contamination, particularly from lead (Pb^{2+}), poses serious environmental and health risks, thereby driving the need for advanced remediation strategies. In this study, both pristine HKUST-1 and urea-functionalized HKUST-1 (HKUST-1@Urea) were synthesized and systematically compared for Pb^{2+} removal from aqueous solutions. Structural and spectroscopic analyses (XRD, FT-IR, and SEM) confirmed successful urea incorporation, which introduced amino and carbonyl groups that both improve hydrophilicity and increase the density of adsorption sites. Adsorption experiments demonstrated that HKUST-1@Urea outperformed unmodified HKUST-1, achieving 98% Pb^{2+} removal within 45 min and a maximum adsorption capacity of 400 mg g^{-1}, compared to the lower values of HKUST-1. Isotherm modeling indicated favorable monolayer adsorption, while kinetic fitting revealed fast surface interactions described by a pseudo-second-order model. Thermodynamic evaluation further confirmed that the adsorption mechanism was spontaneous ($\Delta G° = -4.29$ to -7.95 kJ mol^{-1}), endothermic ($\Delta H° = +29.48$ kJ mol^{-1}), primarily physisorption-driven ($\Delta H° < 40$ kJ mol^{-1}), and accompanied by increased interfacial disorder ($\Delta S° = +0.118$ kJ mol^{-1} K^{-1}). Notably, HKUST-1@Urea maintained over 90% removal efficiency across multiple cycles, highlighting its excellent stability and reusability. These results establish HKUST-1@Urea as a cost-effective and sustainable adsorbent with strong potential for practical water purification, demonstrating the advantages of post-synthetic urea modification for enhancing MOF performance.

1. Introduction

Water is indispensable for the survival of living organisms, yet its quality is increasingly threatened by anthropogenic activities. Among the numerous environmental challenges, water contamination has emerged as one of the most critical threats to human health and ecological sustainability.[1,2] The pollution of water resources arises from industrial, agricultural, and domestic activities.[3] Wastewater typically contains a complex mixture of toxic and hazardous substances from sewage, commercial practices, industrial operations, and agricultural runoff. In recent years, pollution originating from industrial effluents has become a particularly urgent concern. Industrial

effluents, especially those from the chemical industry, are major sources of heavy metal contamination. Toxic ions such as Pb(II), Cu(II), Hg(II), and Co(II) are of particular concern owing to their persistence, bioaccumulation, and detrimental impacts on human and environmental health.[4,5] Long-term exposure to these metals can lead to severe diseases, ecological imbalances, and irreversible environmental degradation. Conventional remediation approaches—including ion exchange,[6] liquid chromatography,[7] resin-based techniques,[8] and photocatalytic degradation[9]—have shown effectiveness but suffer from limitations such as high costs, high energy consumption, and operational complexity. This situation has created a strong demand for more efficient, economical, and sustainable solutions with rapid response and high selectivity.

Metal–organic frameworks (MOFs) have recently emerged as promising candidates for water purification owing to their exceptional physicochemical properties. MOFs are crystalline, porous materials formed by the self-assembly of inorganic metal ions or clusters with organic ligands.[10,11] Their high surface areas, tunable pore structures, and functionalized frameworks offer significant advantages for adsorption-based applications. By tailoring the composition and synthesis conditions, the structural and chemical properties of MOFs can

[a]Chemistry Department, Faculty of Science, Menoufia University, Shebin El-Kom, 32512, Egypt. E-mail: ahmedphysical90@gmail.com; Tel: +20 1090674437

[b]Department of Chemistry, College of Science, King Faisal University, Al-Ahsa 31982, Saudi Arabia. E-mail: mynassar@kfu.edu.sa; Tel: +966 538871438

[c]Central Laboratory for Environmental Quality Monitoring, National Water Research Centre, Elkanatir, Egypt

[d]Department of Biotechnology, Faculty of Applied Health Science, October 6th University, October 6th City 12585, Egypt

[e]Institute of Intelligent Manufacturing Technology, Shenzhen Polytechnic University, Shenzhen, 518055, P. R. China

be optimized for specific applications, enabling their use in gas storage and separation,[12] catalysis,[13–15] sensing,[16] adsorption,[17–19] magnetism,[20] drug delivery,[21] and bioimaging.[22] Among the various MOFs, HKUST-1—constructed from copper ions and 1,3,5-benzenetricarboxylate (BTC) ligands—has received considerable attention. It crystallizes in a face-centered cubic structure with square-shaped pores and abundant unsaturated metal sites.[23] Owing to these features, HKUST-1 has been widely investigated for catalysis,[24] liquid-phase separation, methane storage, and toxic gas capture.[25,26]

In water treatment, HKUST-1 demonstrates notable adsorption capacity and selectivity. Its large surface area offers ample adsorption sites, while its unsaturated copper centers provide strong binding interactions with contaminants. Furthermore, its adjustable pore size facilitates the capture of molecules of different sizes. A distinct advantage of HKUST-1 is its versatility in removing a wide range of pollutants, including heavy metals (e.g., Pb(II) and Cd(II)) and organic contaminants such as dyes, pesticides, and pharmaceuticals.[27] Lead (Pb(II)), in particular, is a highly toxic pollutant with serious health consequences. The World Health Organization (WHO) has set a provisional guideline value of 10 $\mu g\ L^{-1}$ for Pb(II) in drinking water, highlighting the need to minimize exposure. Elevated lead concentrations are associated with developmental delays, cognitive impairments, reduced IQ, and behavioral disorders in children, while adults may suffer from kidney damage, cardiovascular diseases, reproductive dysfunction, and neurological disorders.[28] Various strategies—including coagulation, filtration, and chemical precipitation—have been employed to remove Pb(II) from water.[29] Adsorption, however, remains one of the most promising techniques, particularly with advanced adsorbents such as activated carbon, ion-exchange resins, and MOFs.[30,31]

In this study, we report the urea modification of HKUST-1 (HKUST-1@Urea) to enhance its performance for Pb(II) removal from aqueous media. Urea functionalization introduces amine groups to the MOF, which improve adsorption by forming coordination bonds with metal ions. The presence of carbonyl groups further contributes to strong interactions, while the enhanced hydrophilicity improves compatibility with aqueous environments and facilitates pollutant capture. Moreover, the modification reduces metal ion leaching from the framework, ensuring long-term stability and minimizing secondary contamination. This approach offers a simple yet effective strategy to improve the adsorption efficiency of HKUST-1 toward Pb(II), thereby advancing its potential application in sustainable water purification.

2. Experimental section

2.1. Synthesis of HKUST-1

HKUST-1 was synthesized following the procedure reported by Liu et al.,[32] with modifications to the method originally described by Rowsell and Yaghi.[33] Briefly, 1,3,5-benzenetricarboxylic acid (H₃BTC) was dissolved in a mixed solvent of ethanol and N,N-dimethylformamide (DMF) (1 : 1, v/v). In a separate flask, copper(II) nitrate trihydrate was dissolved in distilled water. The two solutions were combined, stirred for 10 min, and then transferred into a Teflon-lined stainless-steel autoclave. The autoclave was heated at 100 °C for 10 h and allowed to cool naturally to room temperature. The resulting product was separated, washed with methanol at 70 °C for 3 h, and centrifuged again. Finally, the precipitate was dried at 60 °C and activated in a vacuum oven at 150 °C for 24 h, as illustrated in Fig. 1.

2.2. Synthesis of HKUST-1@Urea

HKUST-1@Urea was prepared through post-synthetic modification. Urea was first melted, and the as-synthesized HKUST-1 crystals were added to the molten urea with continuous mixing to ensure homogeneity. After natural cooling to room temperature, the solid was collected and washed sequentially with distilled water and methanol to remove excess urea. The product was then centrifuged, dried at 60 °C, and activated in a vacuum oven at 150 °C for 24 h, as shown in Fig. 1.
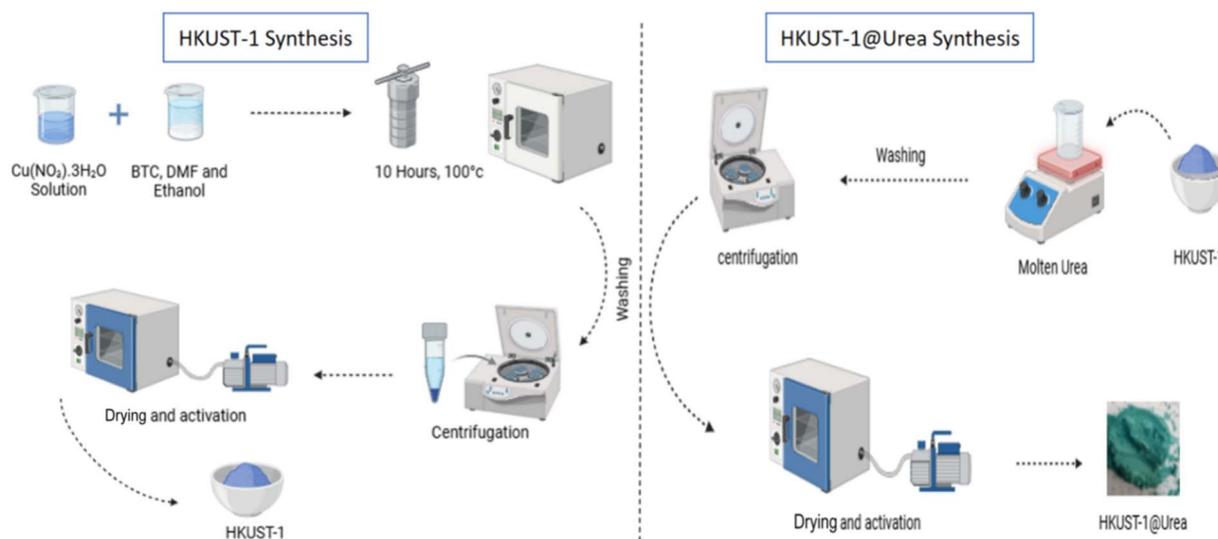

Fig. 1 Schematic of the preparation of HKUST-1 and HKUST-1@Urea.

2.3. Characterization

The adsorbents were characterized by XRD, SEM, FT-IR, BET, and TGA. Powder X-ray diffraction (PXRD) analysis was performed on a Rigaku D/Max-2550 diffractometer furnished with a SolX detector using Cu K radiation with $\lambda = 1.542$ Å. Data were collected by step scanning at $2\theta = 0.02°$ per second from 5° to 50°. The morphology of the catalyst was studied using a SUPRA 55 1 scanning electron microscope (SEM) fitted with an acceleration voltage of 20 kV. Nitrogen sorption experiments were performed at −196 °C on a 3H-2000PS1 gas sorption and porosimetry system. The samples were regularly arranged for examination after degassing at 150 °C for 2 h under vacuum until the final pressure reached 1×10^{-3} torr. Fourier transform infrared (FT-IR) spectroscopy was performed on a Nicolet iS10 spectrometer. Spectra were recorded with the KBr pellet technique using a Bruker Equinox 55 Fourier transform infrared spectrophotometer, and diffuse reflectance spectra were scanned in the range of 500–4000 cm^{-1} with a resolution of 2 cm^{-1} with 100 scans in each measurement. Thermogravimetric analysis (TGA) was conducted on Shimadzu TA-50. X-ray photoelectron spectroscopy (XPS) was carried out using monochromatic X-ray Al K-alpha radiation on a US Thermo-Scientific K-alpha apparatus. The ^{1}H NMR spectra were recorded on a Bruker Advance 400 MHz spectrometer using a digested deuterated mixture as the solvent at room temperature; the chemical shifts (δ) are expressed in ppm.

2.4. Lead ion adsorption study

The adsorption performances of HKUST-1 and HKUST-1@Urea toward Pb^{2+} ions were evaluated using an aqueous solution containing Pb^{2+} as a model pollutant. In each experiment, 25 mg of the adsorbent was added to 50 mL of a Pb^{2+} solution (100 mg L^{-1}) prepared from lead(II) nitrate. The suspension was shaken at 150 rpm for 45 min and then filtered. The residual concentration of Pb^{2+} ions was determined by inductively coupled plasma (ICP) analysis. The adsorption capacity (Q_t) and removal efficiency (% R) were calculated according to eqn (1) and (2), respectively:

$$Q_t = \frac{(C_0 - C_t)V}{m} \tag{1}$$

$$\%\ R = \frac{(C_0 - C_t)}{C_0} \times 100 \tag{2}$$

The adsorption capacity (Q_t) is expressed in milligrams per gram (mg g^{-1}), while the removal efficiency (% R) represents the effectiveness of the process. C_0 (mg L^{-1}) and C_t (mg L^{-1}) denote the initial and equilibrium concentrations of Pb^{2+} ions in the solution, respectively. V (L) represents the volume of the solution, and m (g) indicates the mass of the adsorbent.

3. Results and discussion

3.1. Synthesis and characterization of the HKUST-1 and HKUST-1@Urea MOFs

HKUST-1 was successfully synthesized *via* a solvothermal route, yielding uniform blue crystals, consistent with previous
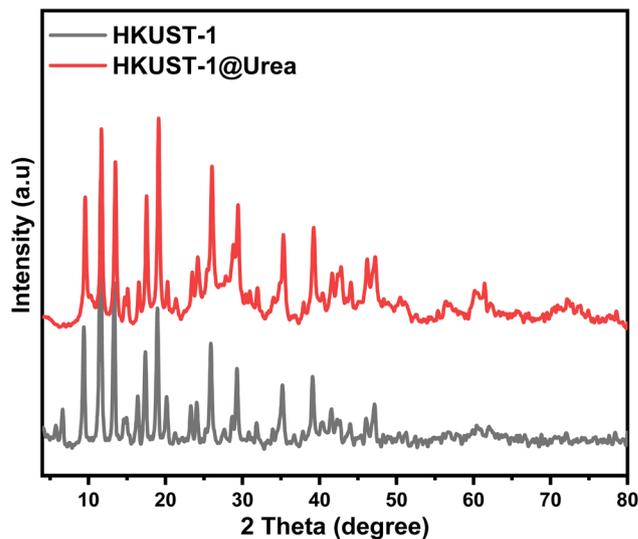

Fig. 2 XRD patterns of HKUST-1 and HKUST-1@Urea adsorbents.

reports.[32,33] The post-synthetic modification with urea was achieved by direct incorporation into molten urea, which preserved the overall MOF. The successful preparation of both HKUST-1 and HKUST-1@Urea was confirmed through structural and morphological characterizations.

The XRD patterns in Fig. 2 illustrate the crystalline structures of HKUST-1 and HKUST-1@Urea. The black curve represents HKUST-1, showing sharp and distinct peaks indicative of a well-defined crystalline structure. The red curve, corresponding to HKUST-1@Urea, exhibits broader and less distinct peaks compared to HKUST-1, suggesting a decrease in crystallinity due to urea incorporation. The presence of urea likely caused partial amorphization or disorder in the HKUST-1 framework. The intensity of the peaks in HKUST-1@Urea is also generally lower than that in pure HKUST-1, further indicating a reduction in crystallinity. The main peaks in both patterns align at similar 2θ values, confirming that the basic framework of HKUST-1 is retained even after urea modification. The differences in peak intensities and widths highlight the impact of urea on the structural properties of HKUST-1.

The nitrogen sorption isotherms of HKUST-1 and HKUST-1@Urea, depicted in Fig. 3a, provide insights into their surface area and porosity characteristics. HKUST-1 exhibits a typical type I isotherm, indicative of microporous materials with high adsorption capacities at low relative pressure. Its surface area is 1352 m^2 g^{-1}, and its pore volume is 0.76 cm^3 g^{-1}. By contrast, for HKUST-1@Urea, the BET surface area is 90 m^2 g^{-1}, and the total pore volume is 0.23 cm^3 g^{-1}, with an average pore diameter of 12.7 nm. The high adsorption volume of HKUST-1 is consistent with its well-known high surface area and microporous structure. HKUST-1@Urea, however, shows a markedly different sorption behavior, with significantly lower adsorption volumes across all relative pressures, not exceeding 100 cm^3 g^{-1}. The initial adsorption at low pressures is minimal, indicating a reduction in microporosity. The gradual increase in adsorption at higher relative pressures suggests the presence of
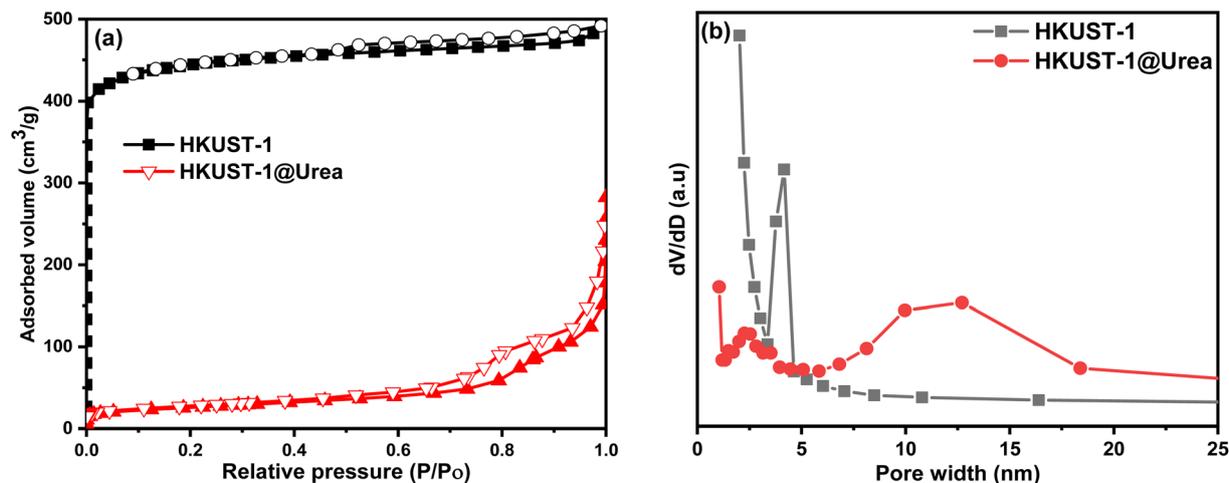
Fig. 3 N_2 sorption isotherms (a) and pore size distributions (b) of HKUST–1 and HKUST–1@Urea adsorbents.

mesopores or larger pores introduced *via* the incorporation of urea, as presented in Fig. 3b. The reduction in the overall adsorption capacity of HKUST-1@Urea implies that urea incorporation disrupts the original microporous structure, likely due to partial pore blockage or framework deformation. This transformation leads to a mixed micro- and mesoporous structure, as evidenced by the isotherm's shape and pore size distribution.[34] These observations align with the SEM and TGA results, highlighting that urea incorporation significantly alters the physical structure of HKUST-1, impacting its surface area and porosity. Such modifications can affect the material's performance in applications like adsorption and catalysis, where the surface area and pore structure are critical parameters.

The SEM images in Fig. 4 provide insights into the morphology and particle size differences between HKUST-1 (a) and HKUST-1@Urea (b). The image (a) of HKUST-1 shows well-defined, uniform, and crystalline particles with a regular, polyhedral shape.[35,36] The particle size appears to be relatively large, averaging around 10 μm, indicating a high degree of crystallinity and uniform growth conditions. In contrast, the image (b) of HKUST-1@Urea shows a significant change in the

morphology and particle size. The particles are smaller and less defined and appear to be more aggregated than the pristine HKUST-1. The average particle size of HKUST-1@Urea is around 2 μm, significantly smaller than that of HKUST-1, suggesting that the incorporation of urea disrupts the crystal growth, leading to the formation of smaller particles. Additionally, the mesoporosity in HKUST-1@Urea is evident from the presence of mesopores within the particles, as highlighted by the black circle in the inset of Fig. 4b. These mesopores, which are not present in the pristine HKUST-1, indicate that urea incorporation induces porosity within the material. The orange circle in Fig. 4b highlights regions where particle aggregation occurs, possibly due to the formation of interparticle mesopores.[37] This increased porosity and reduced particle size in HKUST-1@Urea can enhance its textural properties, potentially improving its performance in applications such as adsorption or catalysis. The introduction of mesoporosity and the disruption of the crystalline structure are direct consequences of urea incorporation, which modifies the growth mechanism and morphology of the HKUST-1 framework.

The FT-IR spectra in Fig. 5 provide clear evidence of the successful incorporation of urea into the HKUST-1 framework,
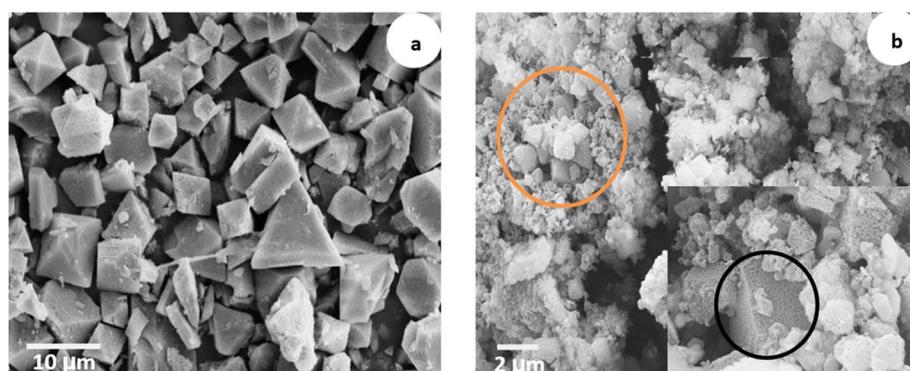

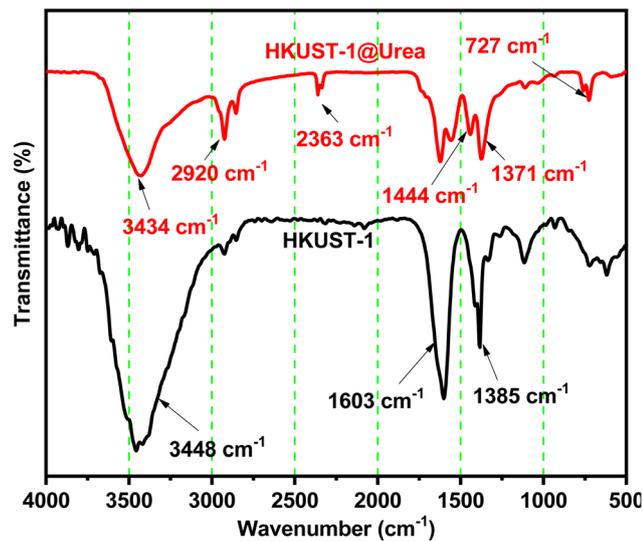**Fig. 4** SEM images of HKUST–1 (a) and (b) HKUST–1@Urea samples.

Fig. 5   FT–IR spectra of HKUST–1 and HKUST–1@Urea samples.

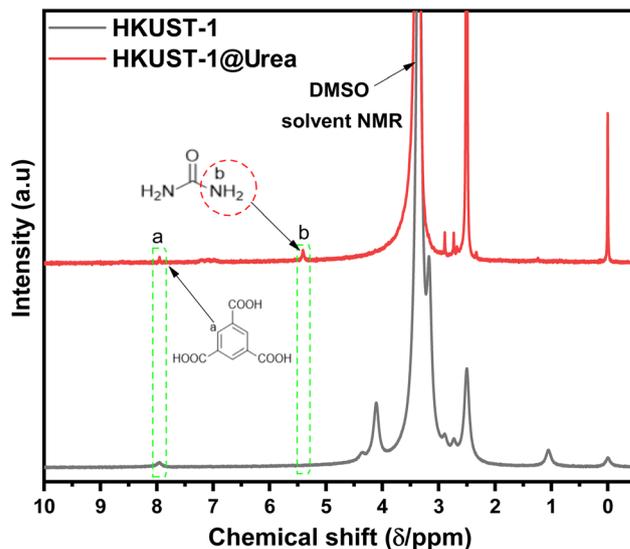Fig. 6 ^{1}H NMR spectra of the HKUST–1 (black) and HKUST–1@Urea (red) samples.

forming the HKUST-1@Urea composite. In the spectrum of pure HKUST-1 (black line), the characteristic bands are observed at 3448 cm^{-1}, corresponding to O–H stretching vibrations from adsorbed water, 1603 cm^{-1} and 1385 cm^{-1}, which are attributed to the asymmetric and symmetric stretching vibrations of the carboxylate groups coordinated to copper nodes in the MOF structure, respectively.[38,39] Upon the formation of the HKUST-1@Urea composite (red line), several new absorption bands emerge, confirming the presence of urea. The prominent band at 3434 cm^{-1} is attributed to N–H stretching from urea, while the 2920 cm^{-1} band corresponds to C–H stretching vibrations.[40,41] The sharp peak at 2363 cm^{-1} may indicate the presence of carbamic acid intermediates or CO$_2$ interactions from slight urea decomposition or reaction at elevated temperatures. The additional peaks at 1444 cm^{-1}, 1371 cm^{-1}, and 727 cm^{-1} are characteristic of C–N stretching, N–H bending, and N–C–N skeletal vibrations from urea molecules, respectively. These new bands, absent in the pristine HKUST-1, confirm that urea has been effectively integrated into or onto the MOF structure, likely through physical encapsulation or interaction with open metal sites or functional groups on the HKUST-1 surface. The lack of significant shifts or disappearance of the original HKUST-1 bands indicates that the MOF's structural integrity is retained during the urea incorporation process.

The ^{1}H NMR spectra in DMSO-d$_6$ show a clear difference between pristine HKUST-1 (black) and urea-modified HKUST-1 (red), as shown in Fig. 6. For pristine HKUST-1, only the characteristic aromatic protons of BTC (linker) appear near $\delta \approx 8.2–8.8$ ppm, confirming the intact framework. After urea modification, additional signals appear in the $\delta \approx 5.5–6.5$ ppm region, consistent with the –NH$_2$ protons of urea, while the aromatic BTC region remains unchanged, indicating that the framework structure is preserved. The identical aromatic pattern, but with new urea-related resonances, confirms the successful incorporation of urea molecules within the MOF. Because the spectra

were obtained from digested samples that were washed before digestion with water and methanol to remove physisorbed urea, these resonances reflect the presence of urea species bound to the Cu^{2+} ion of paddlewheel building blocks or confined in pores rather than physisorbed impurities, supporting the urea functionalization of HKUST-1.

The TGA curves of HKUST-1 and HKUST-1@Urea, shown in Fig. 7, illustrate the thermal stability and decomposition behavior of these materials. The black curve (Fig. 7a) represents HKUST-1, showing three major weight loss steps. The initial weight loss of 14.02% below 100 °C corresponds to the loss of adsorbed water. The second step, with a 7.93% weight loss between 100 °C and 300 °C, likely represents the removal of guest molecules or solvent molecules trapped within the pores. The third significant weight loss of 47.45% between 300 °C and 400 °C indicates the decomposition of the HKUST-1 framework itself.[42] By comparison, the red curve (Fig. 7b), representing HKUST-1@Urea, also shows three primary weight loss steps but with different magnitudes. The initial weight loss of 9.68% below 100 °C again corresponds to the loss of adsorbed water, which is slightly lower than that of HKUST-1 due to the solvent-free preparation method. The second step, showing a 7.76% weight loss between 100 °C and 300 °C, indicates the removal of urea and other volatile components. The major decomposition of the HKUST-1@Urea framework occurs between 300 °C and 400 °C, with a 44.83% weight loss. This indicates that the framework decomposes similarly to HKUST-1 but at a slightly different rate due to urea incorporation. Finally, a minor weight loss of 4.81% is observed up to 500 °C, which might be due to the final decomposition of residual components. The overall thermal stability of HKUST-1@Urea is slightly lower than that of pure HKUST-1, as indicated by the lower total weight loss. These differences in thermal behavior reflect the influence of urea on the thermal properties of the HKUST-1 framework, potentially modifying its application properties.[43]
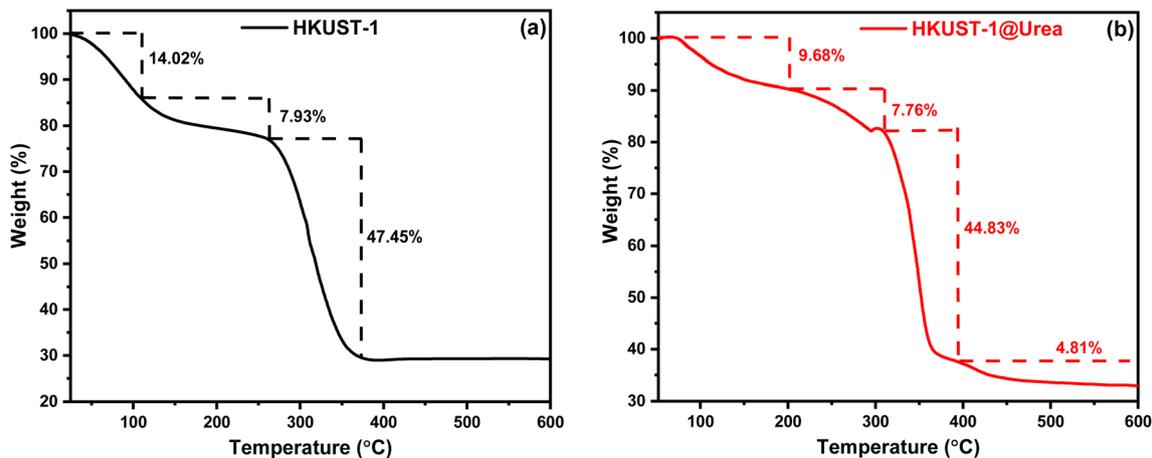
Fig. 7 TGA curves of HKUST-1 (a) and HKUST-1@Urea (b) samples.

3.2. Adsorption properties of HKUST-1 and urea-modified HKUST-1

Adsorption represents a highly effective and economical approach for the removal of toxic metal ions from contaminated water. In the present study, the capacity of HKUST-1 and urea-functionalized HKUST-1 (HKUST-1@Urea) to eliminate Pb^{2+} ions—a hazardous and persistent pollutant—was systematically investigated. The adsorption capacity and removal efficiency were used as the primary metrics to evaluate the suitability of these materials for water purification applications.

3.2.1. Impact of the pH on the adsorption of Pb^{2+} ions.
The pH level of the solution plays a crucial role in enhancing the adsorption capacity for Pb^{2+} ions, as it governs the interactions between the adsorbate molecules and adsorbent particles, thereby influencing the adsorption process in relation to the surface functional groups. To assess the influence of the initial pH on adsorption effectiveness, we examined the pH range from 4 to 6. Our findings reveal that the adsorbent's stability is compromised below pH 4, while precipitation occurs at pH 7.[43,44] The experimental conditions included 50 mg of the adsorbent, 50 mL of a Pb^{2+} ion solution with a concentration of 100 mg L^{-1}, 1 hour of contact time, and room temperature. The resulting data are presented in Fig. 8. As shown in Fig. 8, both HKUST-1 and HKUST-1@Urea exhibit the highest lead ion adsorption efficiency at pH 5, with removal efficiencies reaching approximately 90% and 95%, respectively. At pH 4, the adsorption efficiency of HKUST-1 is around 70%, while HKUST-1@Urea shows a higher efficiency of about 80%, indicating that the presence of urea enhances adsorption at lower pH levels. At pH 6, the removal efficiencies of both materials slightly decrease but remain relatively high, around 80% for HKUST-1 and 85% for HKUST-1@Urea. These results suggest that the optimal pH for lead adsorption on both HKUST-1 and HKUST-1@Urea is around 5, where the surface functional groups are likely most effective in capturing lead ions. The enhanced performance of HKUST-1@Urea at all tested pH levels indicates that urea incorporation improves the material's adsorption capabilities. This may be due to the increased mesoporosity and

altered surface chemistry introduced by urea, as observed in previous characterizations.

3.2.2. Impact of the contact time.
In this experiment, 50 mg of the adsorbent was introduced to a 50 mL solution containing Pb^{2+} ions at a concentration of 100 mg L^{-1} and a pH of 5. The mixture was then shaken at room temperature for varying durations ranging from 5 to 75 min. As shown in Fig. 9, the rate of Pb^{2+} ion adsorption is rapid for both HKUST-1 and HKUST-1@Urea, reaching equilibrium after approximately 45 min. This rapid adsorption can be attributed to the initially vacant binding sites on the adsorbents, which quickly become occupied by lead ions. The removal efficiency (Fig. 9a) of both adsorbents shows a sharp increase in the first 10 min, with HKUST-1@Urea slightly outperforming HKUST-1 in terms of efficiency. Both HKUST-1 and HKUST-1@Urea materials achieve over 90% removal efficiency within 45 min (93% for HKUST-1 and 97% for HKUST-1@Urea). The adsorption
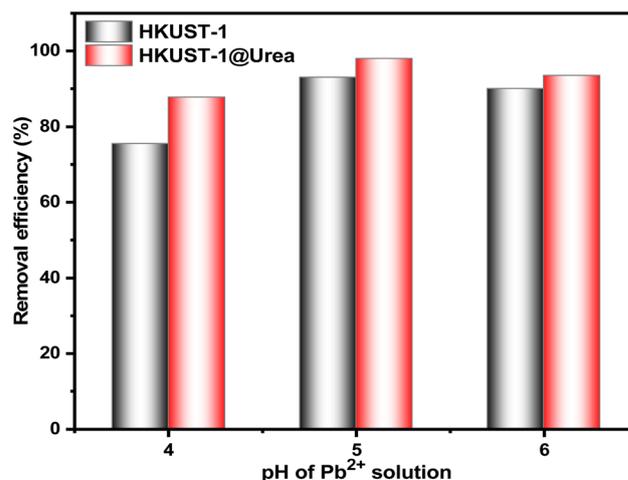

Fig. 8 Effect of the pH on Pb^{2+} ion adsorption on HKUST-1 and HKUST-1@Urea in 50 mL of the lead nitrate solution with a concentration of 100 mg L^{-1}, a contact time of 1 h, and 50 mg of the adsorbent.
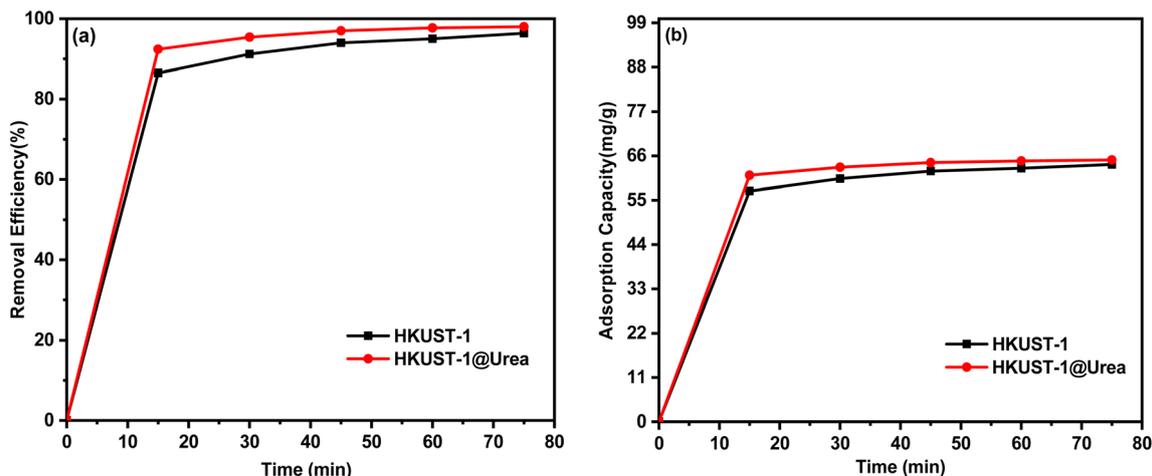
Fig. 9 Effect of the contact time on Pb^{2+} ion adsorption on HKUST-1 and HKUST-1@Urea: (a) removal efficiency and (b) adsorption capacity *versus* time.

capacity (Fig. 9b) also demonstrates a similar trend, with a steep initial increase, followed by a plateau, indicating the saturation of binding sites. HKUST-1@Urea consistently shows a higher adsorption capacity than HKUST-1, likely due to the enriched chelating groups (amine and carbonyl groups) and mesoporosity introduced by urea incorporation. Therefore, for optimal Pb^{2+} ion removal, a contact time of 45 min is recommended, as extending the contact time beyond this point shows a minimal increase in the adsorption efficiency or capacity. The results highlight that both materials are highly efficient for lead ion removal, with HKUST-1@Urea offering marginally better performance. The rapid achievement of equilibrium suggests that these materials are suitable for practical applications where quick and efficient removal of heavy metals is required.

3.2.3. Impact of the adsorbent dose. The effect of the adsorbent dosage on Pb^{2+} ion adsorption was investigated under specific conditions: pH 5, room temperature, 50 mL of a lead solution with a concentration of 100 mg L^{-1}, and a contact time of 45 min. The outcomes, presented in Fig. 10, reveal that the Pb^{2+} removal efficiency increases with increasing adsorbent dosage from 10 mg to 25 mg for both HKUST-1 and HKUST-1@Urea. Beyond 25 mg, the removal efficiency reaches a plateau, indicating that any additional adsorbent does not significantly enhance lead ion removal. At the optimal dosage of 25 mg, both HKUST-1 and HKUST-1@Urea achieve nearly 100% removal efficiency, with HKUST-1@Urea showing a slightly higher efficiency. This plateau suggests that the adsorption sites become saturated at this dosage, and further increases in the adsorbent quantity do not provide additional active sites for Pb^{2+} ion adsorption.[43] The slight advantage of HKUST-1@Urea over HKUST-1 can be attributed to the increased chelating groups and mesoporosity introduced by urea incorporation, providing more accessible adsorption sites.[45] These results align with the behavior observed in other adsorption studies, where an optimal adsorbent dosage is identified, beyond which the removal efficiency does not significantly improve. Overall, the findings demonstrate that 25 mg is the optimal dosage for

both adsorbents under the given experimental conditions. This dosage ensures maximum efficiency while minimizing the amount of material used, making the process more cost-effective and practical for real-world applications.

3.2.4. Impact of the lead ion initial concentration. Various concentrations of aqueous Pb^{2+} ions (10, 30, 50, 70, 100, 130, 150, 170, and 200 mg L^{-1}) were prepared to evaluate the adsorption efficiency of the adsorbents HKUST-1 and HKUST-1@Urea. 25 mg of the adsorbent was added in each solutions, and the solutions were placed in a shaker for 45 minutes at room temperature. The effectiveness of the adsorbents was assessed by measuring the percentage of adsorption and adsorption capacity. The results, depicted in Fig. 11, clearly indicate an initial increase in adsorption efficiency, which then
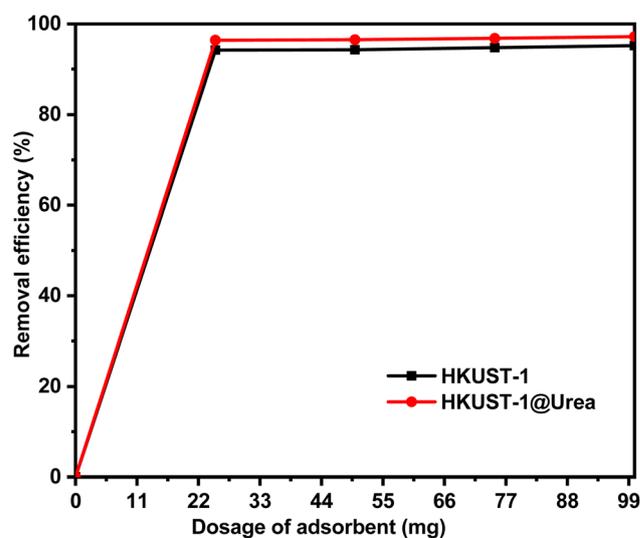

Fig. 10 Effect of the adsorbent dosage on Pb^{2+} ion adsorption on HKUST-1 and HKUST-1@Urea at pH 5, room temperature, 50 mL of a Pb^{2+} ion solution with a concentration of 100 mg L^{-1} and a contact time of 45 min.
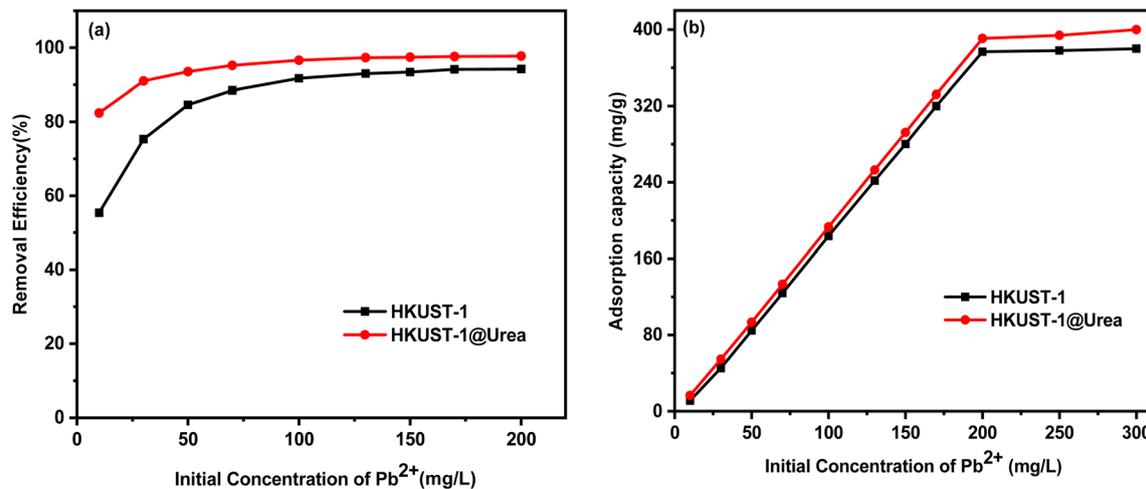
Fig. 11 (a and b) Effect of the lead concentration on Pb^{2+} ion adsorption on HKUST-1 and HKUST-1@Urea at a contact time of 45 min, an adsorbent dose of 25 mg, and pH = 5.

levels off as the Pb^{2+} ion concentration rises from 10 to 100 mg L^{-1}. Fig. 11a shows that the removal efficiency of both HKUST-1 and HKUST-1@Urea increases with the Pb^{2+} ion concentration, reaching a plateau around 90–100 mg L^{-1}. Notably, HKUST-1@Urea consistently demonstrates higher removal efficiency than HKUST-1 at all concentrations, peaking at around 99% removal efficiency. This suggests that urea incorporation enhances the adsorption performance of HKUST-1. Fig. 11b presents the adsorption capacity, which increases linearly with the Pb^{2+} ion concentration for both adsorbents, with HKUST-1@Urea showing slightly higher capacities at higher concentrations. The adsorption capacity of both materials increases from around 20 mg g^{-1} at 10 mg L^{-1} to approximately 70 mg g^{-1} at 150 mg L^{-1}. Based on these findings, it can be inferred that both HKUST-1 and HKUST-1@Urea exhibit greater effectiveness in treating aqueous Pb^{2+} ion solutions with concentrations up to 100 mg L^{-1}. The enhanced performance of HKUST-1@Urea can be attributed to the increased chelating groups and mesoporosity introduced by urea, providing more active sites for Pb^{2+} ion adsorption. These results confirm that both materials are highly efficient for lead removal from water, with HKUST-1@Urea showing superior

performance, making it a promising candidate for practical applications in water treatment.

Based on the comparative data in Table 1, HKUST-1 demonstrates a competitive adsorption capacity for Pb^{2+} (380 mg g^{-1}) relative to other literature-reported adsorbents. It substantially outperforms several materials, including UiO-66 (melamine-modified) (205 mg g^{-1}), Algal biomass *Sargassum glaucescens* (45.8 mg g^{-1}), and zeolite-NaX (14.22 mg g^{-1}). While HKUST-1 exceeds mid-range adsorbents like HCl-activated Aloji clay (333.3 mg g^{-1}), it falls short of the highest-capacity materials such as Tb-based MOFs (nanotube-like) (547 mg g^{-1}) and NH$_2$-MIL-53(Al) (492.4 mg g^{-1}). This positions HKUST-1 as a robust adsorbent, though not the most exceptional in terms of the absolute capacity, among the surveyed MOFs and mineral-based materials.

The urea-functionalized variant, HKUST-1@Urea, exhibits a measurable enhancement in Pb^{2+} adsorption (400 mg g^{-1}) compared to the parent HKUST-1 (380 mg g^{-1}), signifying a 5.3% increase, which is attributable to urea modification. This improvement suggests that urea integration optimizes the material's affinity for Pb^{2+}, potentially through enhanced surface chemistry or porosity. While HKUST-1@Urea still trails

Table 1 Comparison of the performance of HKUST-1 and HKUST-1@Urea with selected adsorbents for Pb^{2+} removal from aqueous solutions reported in the literature

Adsorbent	Metal removal	Max. adsorption capacity (mg g^{-1})	Ref.
Zeolite-NaX	Pb^{2+}	14.22	46
Fe-modified sporopollenin (Fe-Sp) biomass	Pb^{2+}	22.72	47
Algal biomass *Sargassum glaucescens*	Pb^{2+}	45.8	48
UiO-66 (melamine-modified)	Pb^{2+}	205	49
Activated Aloji clay (HCl-activated)	Pb^{2+}	333.3	50
HKUST-1	Pb^{2+}	380	This work
HKUST-1@Urea	Pb^{2+}	400	This work
NH$_2$-MIL-53(Al)	Pb^{2+}	492.4	51
Tb-based MOF (nanotube-like)	Pb^{2+}	547	52

behind Tb-based MOFs (547 mg g^{-1}) and NH$_2$-MIL-53(Al) (492.4 mg g^{-1}), its capacity surpasses other modified materials like melamine-modified UiO-66 (205 mg g^{-1}) and outperforms all non-MOF adsorbents listed (*e.g.*, biosorbents, zeolites, and clay). The modification's efficacy is further underscored when compared with drastically lower-capacity biosorbents such as Fe-modified sporopollenin (22.72 mg g^{-1}). This positions HKUST-1@Urea as a strategically optimized adsorbent within the HKUST series, offering incremental but scientifically significant performance gains for Pb^{2+} remediation.

3.2.5. Adsorption kinetic study. The time-dependent adsorption of metal ions is presented in Fig. 12, conducted at pH 5 for a Pb^{2+} ion solution. The maximum adsorption is observed within 75 minutes, indicating that HKUST-1 and HKUST-1@Urea exhibit rapid adsorption kinetics. The adsorption data *versus* time were analyzed using two simplified kinetic models: the pseudo-first-order and pseudo-second-order models. The models are computed by eqn (3) and (4), respectively:[53,54]

$$\log(q_e - q_t) = \log q_e - \left(\frac{k_1}{2.303}\right)t \tag{3}$$

$$\frac{t}{q_t} = \frac{1}{k_2 q_{e2}} + \frac{t}{q_e} \tag{4}$$

where k_1 and k_2 are the rate constants of the pseudo-first-order (min^{-1}) and the pseudo-second-order models of adsorption (g mg^{-1} min^{-1}), respectively, and q_e and q_t (mg g^{-1}) refer to the amount of the metal ion adsorbed at equilibrium and at time t, respectively. The kinetic parameters were obtained by applying the pseudo-first-order and pseudo-second-order kinetic models. The linear plots of $\log(q_e - q_t)$ *versus* t for the pseudo-first-order model and t/q_t *versus* t for the pseudo-second-order model were constructed to evaluate their applicability. The suitability of each model was assessed based on the correlation coefficients (R^2) and the agreement between the experimentally measured and theoretically calculated q_e values. As presented in Fig. 12

and Table 2, the pseudo-second-order model exhibits the highest R^2 values and the closest alignment of q_e values, confirming that this model best describes the adsorption behavior of Pb^{2+} onto HKUST-1@Urea. These findings suggest that the adsorption kinetics are primarily controlled by surface interaction processes between Pb^{2+} ions and active sites on the modified MOF.

The data do not align with the pseudo-first-order model, as evidenced by the discrepancy between the calculated q_e values and those determined experimentally (Table 1). This suggests that the adsorption process likely involves a multistep mechanism, including (i) external film diffusion, (ii) intraparticle diffusion, and (iii) interactions between the adsorbate and active sites. To identify the rate-determining step, the adsorption data were analyzed in accordance with the Fickian diffusion law (eqn (5)):

$$q_t = x + K_i t^{0.5} \tag{5}$$

where q_t is the amount of the metal ion adsorbed at time t, K_i is the intraparticle diffusion rate constant (mg g^{-1} min$^{-0.5}$), and x represents the boundary layer diffusion effects. As the value of x decreases, the effect of boundary layer diffusion decreases. The plot of q_t *vs.* $t^{0.5}$ (Fig. 13) gives a straight line that does not pass through the origin; this indicates that the adsorption reaction is controlled by intraparticle diffusion along with boundary layer diffusion.[55]

3.2.6. Adsorption isotherm study. The study of adsorption isotherms is important for obtaining the main information about the mechanism of the adsorption process and interactions between HKUST-1 and HKUST-1@Urea as adsorbents and Pb^{2+} ions as the adsorbate.[56] In this study, the experimental data of Pb^{2+} ion adsorption onto the HKUST-1 and HKUST-1@Urea surfaces were fitted with the three most applied isotherm models, namely, Langmuir, Freundlich, and Dubinin–Radushkevich (D–R) isotherm models. Adsorption isotherms were
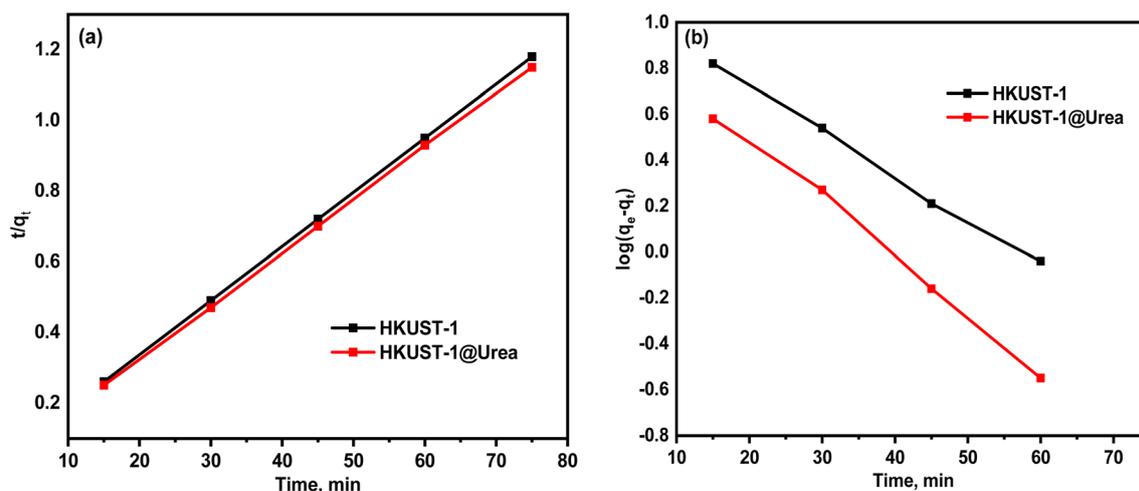

Fig. 12 Pseudo-second-order kinetics (a) and pseudo-first-order kinetics (b) of the uptake of Pb^{2+} ions on HKUST-1 and HKUST-1@Urea adsorbents.

Table 2 Kinetic model parameters for Pb^{2+} ion adsorption on HKUST-1 and HKUST-1@Urea adsorbents

Adsorbent	$q_{e(exp.)}$ (mg g^{-1})	Pseudo-first-order			Pseudo-second-order		
		k_1 (min^{-1})	$q_{e(cal.)}$ (mg g^{-1})	R^2	k_2 (g mg^{-1} min^{-1})	$q_{e(cal.)}$ (mg g^{-1})	R^2
HKUST-1	63.84	0.045	12.88	0.996	0.0078	65.23	1
HKUST-1@Urea	65	0.059	9.77	0.994	0.0102	66.67	0.999
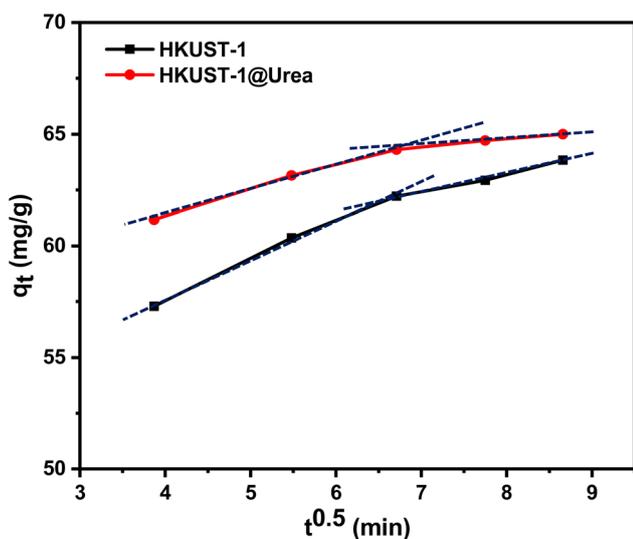
Fig. 13 Intraparticle diffusion kinetics of Pb^{2+} ion uptake on HKUST-1 and HKUST-1@Urea.

applied by changing the initial metal ion concentration in the range of 10–200 mg L^{-1} under optimum studied conditions.

3.2.6.1. Langmuir isotherm model. The Langmuir adsorption isotherm[57] is applied to describe equilibrium adsorption under the assumptions of monolayer adsorption onto a homogeneous surface with a fixed number of conformable sites, and maximum adsorption happens when the adsorbate covers the surface; a specific number of accessible sites are available on the adsorbent surface, and all of them have the same energy; the

adsorption process is reversible; monolayer adsorption takes place; and there are no side interactions between the adsorbates. The linearized form of the Langmuir isothermal model can be applied using eqn (6):

$$\frac{C_e}{q_e} = \frac{1}{bq_m} + \frac{C_e}{q_m} \tag{6}$$

where C_e is the concentration of Pb^{2+} ions remaining in the solution at equilibrium (mg L^{-1}), q_e is the amount of Pb^{2+} ions adsorbed per mass unit of the adsorbent at equilibrium (mg g^{-1}), q_m is the maximum adsorption capacity, refers to complete monolayer adsorption (mg g^{-1}), and b is the Langmuir binding constant responsible for the heat of adsorption (L mg^{-1}). Fig. 14a and b shows a plot of C_e/q_e *versus* C_e, which gives a straight-line representation of the Langmuir isotherm model. $(1/bq_m)$ and $(1/q_m)$ can be determined from the intercept and slope of the graph, respectively, as exhibited in Table 3. It was observed that the correlation coefficients R^2 had values of 0.9996 and 0.9997 for Pb^{2+} ions with the maximum adsorption capacities of 383 and 401 mg g^{-1} for HKUST-1 and HKUST-1@Urea, respectively. The coefficient b in the Langmuir equation was a measure of the stability of the complex formed between the Pb^{2+} ions and HKUST-1 and HKUST-1@Urea under experimental conditions. In this study, the small b values of 1.3 and 1.5 L mg^{-1} for Pb^{2+} ions, respectively, were obtained, which indicate the strong binding of Pb^{2+} ions to HKUST-1 and HKUST-1@Urea surfaces. The small value of b obtained for HKUST-1, compared to that of HKUST-1@Urea, indicated that Pb^{2+} ions formed the strongest binding with the HKUST-1@Urea surface. This can also be proved by the high
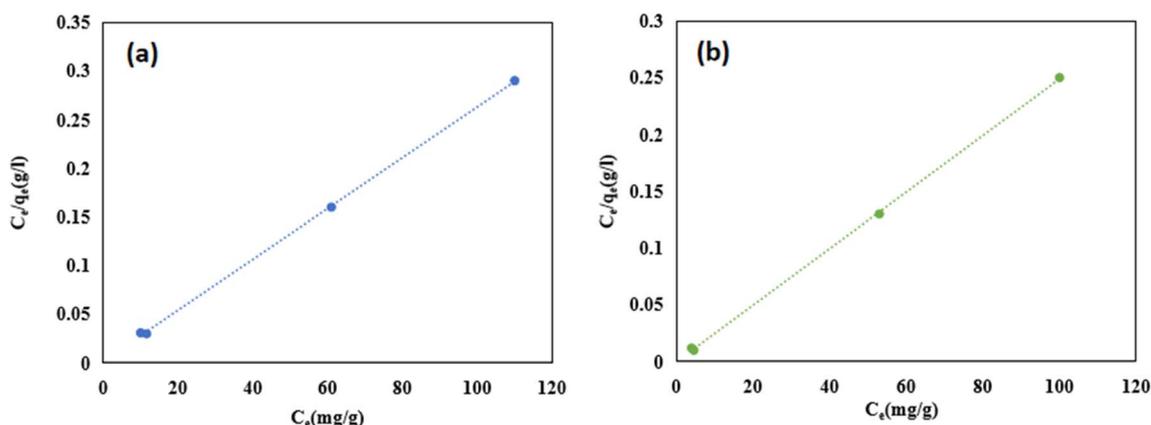

Fig. 14 Langmuir model of Pb^{2+} ions adsorbed onto (a) HKUST-1 and (b) HKUST-1@Urea under the studied optimum conditions.

Table 3 Different isothermal parameters for Pb^{2+} ion adsorption onto HKUST-1 and HKUST-1@Urea

	Parameters								
	Langmuir isotherm parameters				Freundlich isotherm parameters			D–R isotherm parameters	
Samples	$q_{m(exp.)}$ (mg g^{-1})	$q_{m(cal.)}$ (mg g^{-1})	R^2	b (L mg^{-1})	K_F (mg g^{-1}) (L mg^{-1})$^{1/n}$	R^2	n	E (kJ mol^{-1})	R^2
HKUST-1	383	380	0.9996	1.3	33	0.9461	1.80	0.186	0.985
HKUST-1@Urea	401	400	0.9997	1.5	40	0.9486	1.88	0.438	0.988

adsorption capacity obtained for HKUST-1@Urea, which was higher than that of HKUST-1.[58]

3.2.6.2. Freundlich isotherm. The Freundlich equation explains physicochemical adsorption on heterogeneous surfaces.[59] The Freundlich adsorption isotherm is the most used mathematical model for aqueous systems. This isotherm can be applied by eqn (7):

$$q_e = K_F C_0 \frac{1}{n} \qquad (7)$$

The linearized form of the Freundlich isotherm can be applied by eqn (8)

$$\log q_e = \log K_F + \frac{1}{n} \log C_e \qquad (8)$$

where q_e is the amount adsorbed per unit weight of the adsorbent at equilibrium (mg g^{-1}), C_e is the equilibrium concentration of the adsorbate in a solution after adsorption (mg g^{-1}), K_F is an empirical Freundlich constant or capacity factor [(mg g^{-1}) (L mg^{-1})$^{1/n}$], and $(1/n)$ is the Freundlich exponent (the amount of variation in affinity for the adsorbate with a variation in the adsorption density), which varies with the degree of heterogeneity. Fig. 15a and b shows a plot of $\log C_e$ against $\log q_e$, which gives a straight-line representation of the Freundlich isotherm model. $1/n$ and $\log K_F$ can be determined from the slope and intercept of the graph, respectively, as displayed in Table 3. When $1/n = 1$, the isotherm is linear, and the system has constant free energy at all adsorbate concentrations. When $1/n < 1$, the isotherm is concave, and sorbates have weaker free energy, which is favorable for adsorption. It can be observed

that the n values of HKUST-1 and HKUST-1@Urea adsorption were 1.8 and 1.88, respectively. It is obvious that $1/n$ values lie in the range between 0 and 1, which shows the good chemisorption of Pb^{2+} ions onto HKUST-1 and HKUST-1@Urea. The correlation coefficients R^2 had values of 0.9461 and 0.9486 for Pb^{2+} ions, respectively.

3.2.6.3. Dubinin–Radushkevich (D–R) isotherm. The Dubinin–Radushkevich (D–R) isotherm model is more general than the Langmuir isotherm because it does not require a homogeneous surface or a fixed adsorption potential. It is utilized to determine the nature of the sorption process, physical or chemical, and calculate the mean energy of sorption.[60] The Dubinin–Radushkevich isotherm equation[61] is shown by eqn (9):

$$\ln q_e = \ln q_m - \beta \varepsilon^2 \qquad (9)$$

where q_e is the amount of the adsorbate adsorbed at equilibrium (mg g^{-1}), q_m is the amount of the adsorbate adsorbed at the maximum saturation (mg g^{-1}), β is a constant related to the adsorption energy (mol^2 K^{-1} J^{-2}), and ε is the Dubinin–Radushkevich isotherm constant assigned to the potential energy of Polanyi (kJ mol^{-1}), which can be calculated by eqn (10):

$$\varepsilon = RT \ln(1 + 1/C_e) \qquad (10)$$

where R is the molar gas constant, equal to 8.314 J mol^{-1} K^{-1}, T is the adsorption temperature (room temperature = 298 K), and C_e is the concentration of metal ions at equilibrium at different
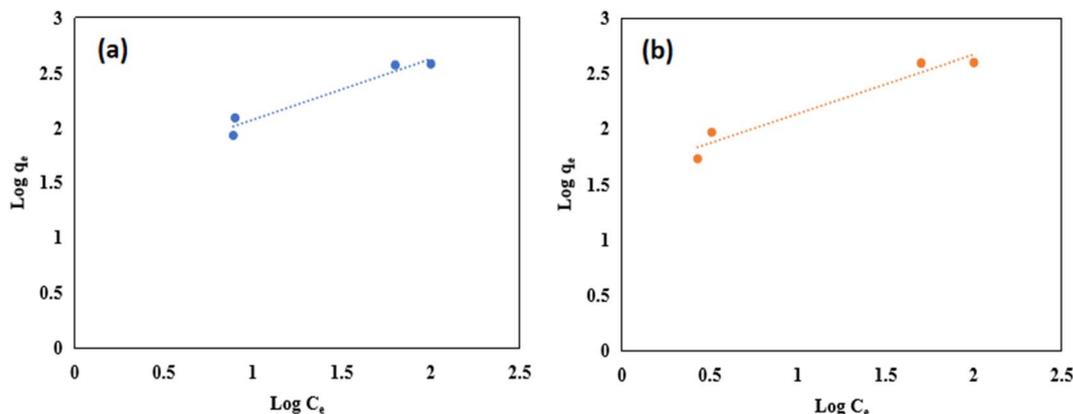

Fig. 15 Freundlich model of Pb^{2+} ions adsorbed onto HKUST-1 (a) and HKUST-1@Urea (b) under the studied optimum conditions.
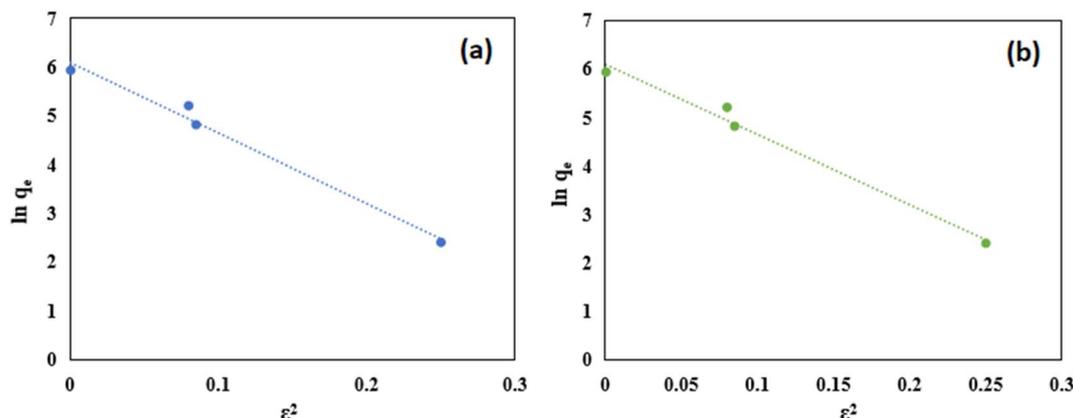
Fig. 16 Dubinin–Radushkevich (D–R) model of Pb^{2+} ions adsorbed onto HKUST-1 (a) and HKUST-1@Urea (b) under optimum adsorption conditions.

initial metal ion concentrations (mg L^{-1}). Fig. 16 shows a plot of ln q_e *versus* ε^2, which gives a straight-line representation of the Dubinin–Radushkevich isotherm model. β and q_m can be determined from the slope and intercept of the graph, respectively, as displayed in Table 3. The mean free energy (E) of sorption can be computed using eqn (11):

$$E = \frac{1}{\sqrt{2\beta}} \qquad (11)$$

where E (kJ mol^{-1}) gives information about how the adsorption process occurs, physically or chemically. If E values lie between 8 and 16 kJ mol^{-1}, the adsorption process takes place chemically, and if E is less than 8 kJ mol^{-1}, the adsorption process proceeds physically.[62] It was observed that the energy value (E) was equal to 0.186 kJ mol^{-1} for HKUST-1 and 0.438 kJ mol^{-1} for HKUST-1@Urea; therefore, the process of the adsorption of Pb^{2+} ions on both HKUST-1 and HKUST-1@Urea was physisorption.[63] The q_m values for HKUST-1 and HKUST-1@Urea, calculated using the Dubinin–Radushkevich model curves, were obtained as 403 mg g^{-1} ($R^2 = 0.985$) and 437 mg g^{-1} ($R^2 = 0.988$), respectively. It was observed that the Langmuir isotherm was a better fitting model than the Freundlich isotherm model and Dubinin–Radushkevich (D–R) model for the adsorption system. Thus, the adsorption of Pb^{2+} ions onto HKUST-1 and HKUST-1@Urea follows the monolayer physisorption process.[64]

3.2.7. Temperature effect and thermodynamic analysis. Temperature significantly affects the adsorption performance by altering adsorbate mobility and adsorbent surface interactions. To investigate this influence, Pb^{2+} adsorption experiments were conducted at four temperatures (288, 298, 308, and 318 K) under optimized conditions. The study reveals that the adsorption capacity of both HKUST-1 and HKUST-1@Urea increases with increasing temperature, confirming that the adsorption process is endothermic.

To further elucidate the adsorption feasibility and mechanism, the thermodynamic parameters Gibbs free energy ($\Delta G°$), enthalpy ($\Delta H°$), and entropy ($\Delta S°$) were determined using eqn (12)–(14):[65,66]

$$\ln K_c = \Delta S°/R - \Delta H°/RT \qquad (12)$$

$$\Delta G° = \Delta H° - T\Delta S° \qquad (13)$$

where R is the universal gas constant (8.314×10^{-3} kJ mol^{-1} K^{-1}), and T is the absolute temperature in Kelvin. The equilibrium constant K_c was calculated from the partition constant K_p, according to Niwas *et al.*[67] To obtain K_p, a plot of $\ln(C_s/C_e)$ *versus* C_s was constructed, and C_s was extrapolated to zero,[68] where C_e is the equilibrium concentration in a solution and C_s is the concentration of Pb^{2+} on the adsorbent surface. Additionally, $\Delta G°$ was validated using eqn (14):

$$\Delta G° = -RT \ln K_c \qquad (14)$$

The linear van't Hoff plots of $\ln K_c$ *versus* $1/T$ (Fig. 17a and b) yield $\Delta H°$ and $\Delta S°$ values, which are summarized along with the $\Delta G°$ values in Table 4. Both HKUST-1 and HKUST-1@Urea exhibit positive $\Delta H°$ values of 25.483 kJ mol^{-1} and 29.481 kJ mol^{-1}, respectively, indicating that Pb^{2+} ion adsorption is endothermic, and higher temperatures promote ion uptake. The positive $\Delta S°$ values (0.102 and 0.118 kJ mol^{-1} K^{-1}, respectively) suggest increasing disorder at the solid–liquid interface due to the improved dispersion of Pb^{2+} ions on active binding sites. Moreover, $\Delta G°$ is negative at all temperatures, ranging from -3.897 to -7.10 kJ mol^{-1} (HKUST-1) and -4.290 to -7.949 kJ mol^{-1} (HKUST-1@Urea), confirming the spontaneous nature of adsorption. The increasing magnitude of $\Delta G°$ with temperature further demonstrates that adsorption becomes more thermodynamically favorable at elevated temperatures. Because $\Delta H°$ values lie well below the 40 kJ mol^{-1} threshold and $\Delta G°$ falls within the -20 to 0 kJ mol^{-1} range, the adsorption of Pb^{2+} ions onto both adsorbents is predominantly driven by physisorption forces.[69] The slightly higher $\Delta H°$, more negative $\Delta G°$, and larger $\Delta S°$ values for HKUST-1@Urea verify that urea functionalization enhances Pb^{2+} affinity, which is attributed to the introduction of amide ($-NH_2$ and $C=O$) functionalities that contribute additional coordination sites and surface interactions.

3.2.8. Effect of coexisting metal ions on Pb^{2+} adsorption. The influence of coexisting metal ions (Zn^{2+}, Cd^{2+}, and Ni^{2+}) on the adsorption behavior of Pb^{2+} onto pristine HKUST-1 and
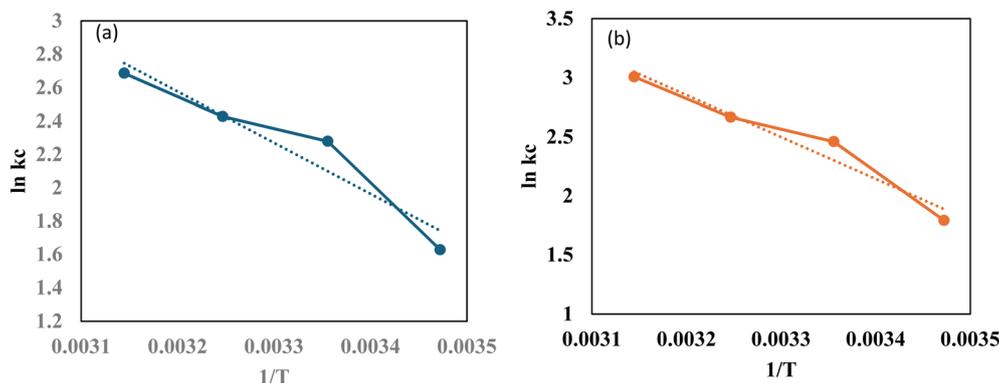
Fig. 17 Plot of ln K_c versus $1/T$ for HKUST-1 (a) and HKUST-1@Urea (b).

Table 4 Thermodynamic parameters for the uptake of Pb^{2+}

	ΔH (kJ mol^{-1})	ΔS (kJ mol^{-1} K^{-1})	ΔG (kJ mol^{-1}) at temperatures			
			288 K	298 K	308 K	318 K
HKUST-1	25.483	0.102	−3.897	−5.645	−6.216	−7.10
HKUST-1@Urea	29.481	0.118	−4.290	−6.093	−6.828	−7.949

HKUST-1@Urea was systematically examined, and the corresponding results are illustrated in Fig. 18. The data reveal that the presence of competing cations in the solution noticeably affects the adsorption efficiency of Pb^{2+}; however, HKUST-1@Urea consistently demonstrates a superior removal performance to the unmodified framework. In conclusion, although the coexistence of other divalent cations slightly suppresses Pb^{2+} uptake due to competitive adsorption, HKUST-1@Urea retains a distinctly higher selectivity toward Pb^{2+}. This superior performance highlights the potential of the modified framework for efficient lead removal from multicomponent aqueous systems containing various heavy metal contaminants.

3.2.9. Reusability study. The recyclability and stability of HKUST-1 and HKUST-1@Urea for Pb^{2+} removal were evaluated through repeated adsorption cycles under optimum conditions.
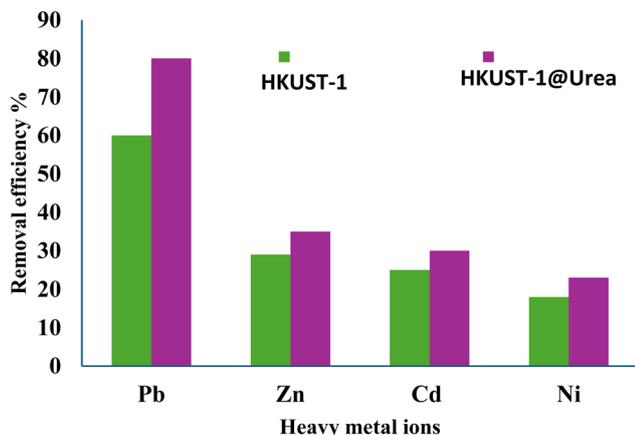

Fig. 18 Effect of coexisting metal ions on Pb^{2+} adsorption by HKUST-1 and HKUST-1@Urea.

Both materials showed high initial removal efficiency, with HKUST-1@Urea performing slightly better due to additional binding sites and improved surface chemistry from urea incorporation (Fig. 19a). Over multiple cycles, a gradual decline in efficiency was observed, likely caused by partial site saturation and minor structural changes. However, HKUST-1@Urea consistently maintained higher performance and stability than pristine HKUST-1. By the fifth cycle, both materials showed reduced efficiency but retained moderate reusability. Overall, urea modification enhanced the durability and regeneration ability of HKUST-1, making it a more promising candidate for long-term Pb^{2+} ion removal in wastewater treatment. The XRD patterns of HKUST-1 and urea-modified HKUST-1 (both fresh and after five adsorption cycles) showed that the crystalline framework of the MOFs remained largely preserved after reuse (Fig. 19b). After five adsorption cycles (spent samples), both materials retained their main diffraction features, demonstrating excellent structural stability under repeated use in Pb^{2+} removal. However, the spent samples (particularly HKUST-1 without urea) showed broader peaks and lower intensities, indicating partial framework degradation or amorphization after multiple exposures to aqueous solutions and metal ion exchange. In contrast, HKUST-1@Urea (spent) retained sharper peaks and better relative intensities, implying that urea functionalization enhanced the chemical stability and rigidity of the framework during cycling, likely by forming hydrogen-bonding networks or reducing Cu^{2+} site leaching.

3.2.10. Mechanistic analysis. The XPS analysis provides clear evidence of the successful adsorption of Pb^{2+} ions onto the HKUST-1@Urea framework (Fig. 20). The survey spectra confirm the presence of Pb after adsorption through the appearance of distinct Pb 4f signals (Fig. 20a), while the persistence of Cu, O, C, and N peaks indicates that the parent structure of HKUST-1@Urea
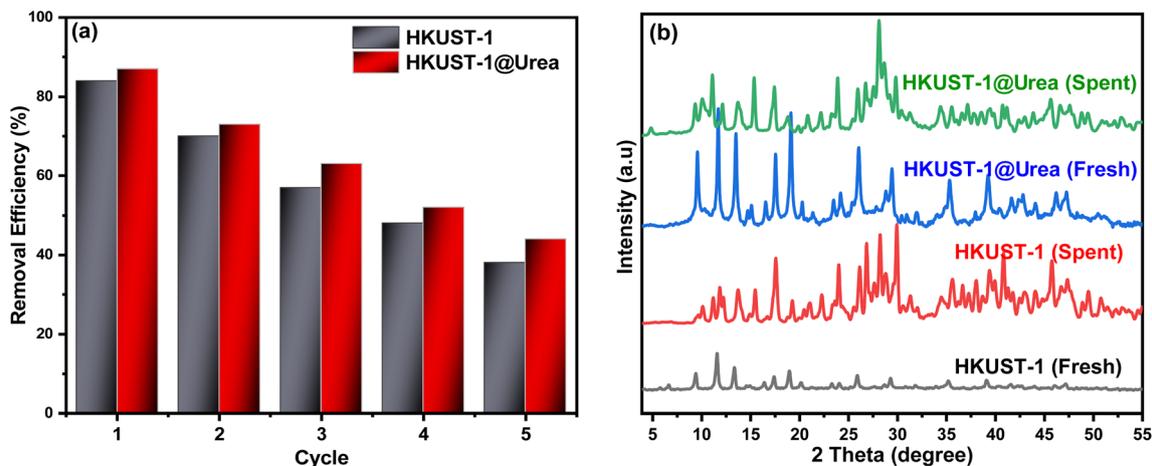
Fig. 19 Reusability of HKUST-1 and HKUST-1@Urea adsorbents in the removal of Pb^{2+} ions from aqueous solutions (a) and XRD patterns of the adsorbent after reuse (b).

remains stable during the process. A closer inspection of the high-resolution spectra provides important insights into the adsorption mechanism. The O 1s spectra show significant shifts in the binding energy after Pb^{2+} adsorption (Fig. 20c), suggesting that oxygen atoms from the carboxylate groups of HKUST-1 and from urea functionalities play a key role in Pb^{2+} coordination. This implies the formation of strong Pb–O bonds that anchor Pb^{2+} within the framework. Similarly, the N 1s spectra exhibit a clear shift to higher binding energies after adsorption (Fig. 20e), indicating that the nitrogen atoms of urea moieties are directly

involved in the coordination process. The interaction of Pb^{2+} with the lone-pair electrons on nitrogen supports the formation of Pb–N bonds, which strengthen the overall binding affinity of the adsorbent. Although the Cu 2p spectra remain largely unchanged (Fig. 20b), minor variations in satellite features suggest that the presence of Pb^{2+} may slightly perturb the local environment of the Cu–O clusters. However, this effect is less significant compared to the strong coordination observed with oxygen and nitrogen atoms. Overall, these results confirm that Pb^{2+} adsorption on HKUST-1@Urea occurs mainly through the synergistic action of oxygen
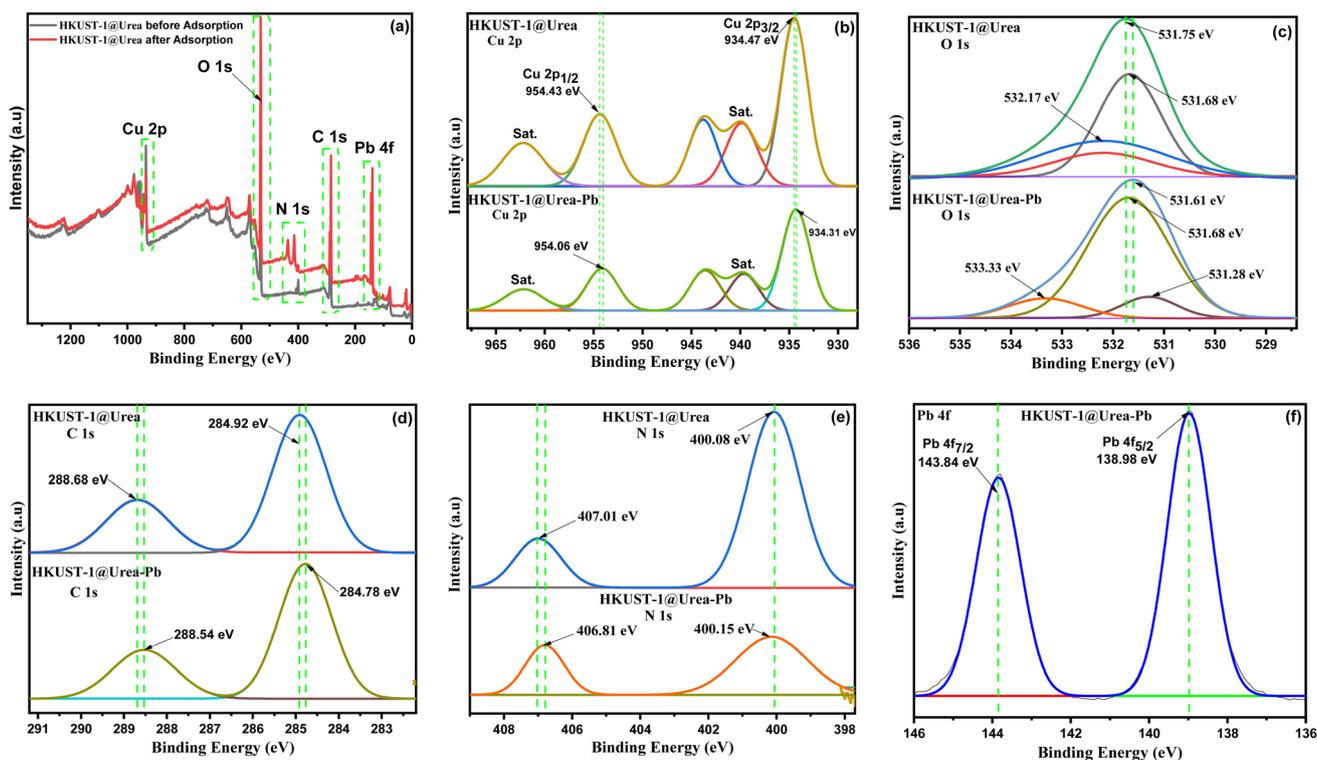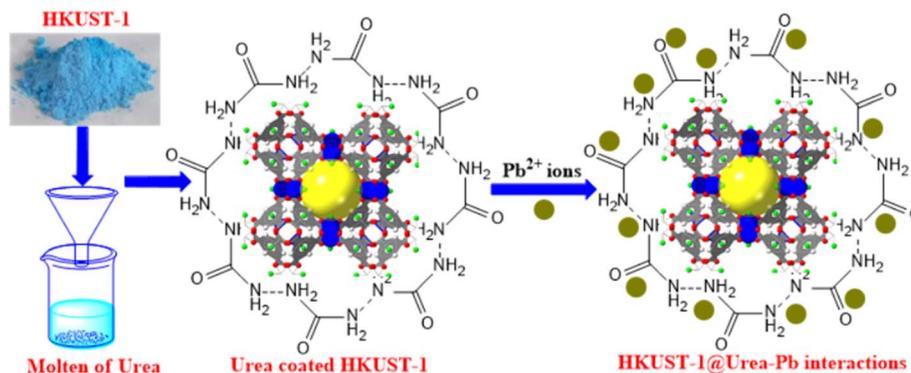

Fig. 20 XPS results of HKUST-1@Urea before and after Pb^{2+} adsorption: (a) XPS survey spectra, (b) Cu 2p spectra; (c) O 1s spectra; (d) C 1s spectra; (e) N 1s spectra; and (f) Pb 4f spectra.

Scheme 1 HKUST-1@Urea preparation procedure and the proposed adsorption mechanism for Pb(II).

and nitrogen donor atoms, which provide multiple high-affinity binding sites. This dual interaction mechanism enhances the stability of Pb^{2+} within the framework and highlights the crucial role of urea modification in improving the adsorption capacity of HKUST-1 for toxic heavy metal ions.

The adsorption of Pb^{2+} ions onto HKUST-1@Urea can be understood through a synergistic mechanism involving structural modification, surface functionalization, and multisite coordination. As illustrated in Scheme 1, the molten-urea treatment coats the HKUST-1 framework with urea functionalities, introducing abundant $-NH_2$ and $C=O$ groups on the MOF surface. These polar sites significantly improve hydrophilicity and provide additional anchoring sites for Pb^{2+} ions.

From a spectroscopic perspective, XPS analysis confirms that both oxygen and nitrogen atoms are actively involved in Pb^{2+} binding. The O 1s spectra show evident binding energy shifts after adsorption, indicating that the carboxylate oxygen from the HKUST-1 linker, as well as the urea-derived carbonyl oxygen, strongly coordinate with Pb^{2+} ions. Simultaneously, the N 1s spectra reveal marked chemical shifts, confirming the contribution of urea's amino groups through lone-pair electron donation, resulting in the Pb–N coordination. These dual interactions form stable Pb–O and Pb–N bonds that enhance affinity and binding strength.

From statistical physics and adsorption fitting perspectives, the high maximum adsorption capacity (400 mg g^{-1}) and excellent fitting with Langmuir-type isotherms suggest a monolayer adsorption process. This implies that Pb^{2+} ions occupy discrete active sites provided by the functionalized surface rather than forming multilayers. Meanwhile, kinetic modeling supports a chemisorption-controlled mechanism, where the rate-limiting step is surface complexation rather than diffusion.

Finally, the recyclability and stability data (>90% efficiency after multiple cycles) confirm that the Pb^{2+} binding is strong yet reversible, indicating that the adsorption occurs through coordination interactions rather than permanent structural degradation of the framework.

4. Conclusions

The urea modification of HKUST-1 successfully enhanced its adsorption performance for Pb^{2+} ion removal from contaminated water. Comprehensive structural and surface analyses (XRD, SEM, FT-IR, BET, and TGA) confirmed the incorporation of urea into the HKUST-1 framework, introducing additional amino and carbonyl functional groups that improved hydrophilicity and provided more active binding sites. As a result, HKUST-1@Urea demonstrated a significantly higher Pb^{2+} adsorption capacity (400 mg g^{-1}) and removal efficiency (98%) under optimized conditions (pH 5, 25 mg of the adsorbent, and 100 mg L^{-1} initial Pb^{2+}). Adsorption behavior was best represented by the Langmuir isotherm, indicating monolayer coverage on a uniform surface. Kinetic analysis followed a pseudo-second-order model, reflecting rapid surface interactions. Thermodynamic results ($\Delta H^\circ < 40$ kJ mol^{-1} and negative ΔG° values) confirmed that Pb^{2+} adsorption was spontaneous, endothermic, and predominantly governed by physisorption forces. Furthermore, the adsorbent retained over 90% efficiency after repeated regeneration cycles, demonstrating excellent stability and reusability. Overall, the post-synthetic functionalization of HKUST-1 with urea offers a cost-effective, highly efficient, and reusable adsorbent for Pb^{2+} remediation. Future work will focus on scaling up production, evaluating performance in complex wastewater matrices, and advancing application in continuous-flow treatment technologies.

Conflicts of interest

There are no conflicts to declare.

Data availability

The data are available at the following link: **https://drive.google.com/drive/folders/1idG3QZb9CPTQggficVVtCU6s7pIEj_DT?usp=sharing**.

Acknowledgements

References

1 Y. Geng, Z. Li, M. Chen, H. Zhao and L. Zhang, The preparation of graphene foam by one-step reduction and air-drying for oil–water separation, *J. Sol-Gel Sci. Technol.*, 2020, **94**, 375–383.

2 S. Dutta, A. Sinelshchikova, J. Andreo and S. Wuttke, Nanoscience and nanotechnology for water remediation: an earnest hope toward sustainability, *Nanoscale Horiz.*, 2024, **9**, 885–899.

3 U. Krishnan, M. Kaur, G. Kaur, K. Singh, A. R. Dogra, M. Kumar and A. Kumar, MoS_2/ZnO nanocomposites for efficient photocatalytic degradation of industrial pollutants, *Mater. Res. Bull.*, 2019, **111**, 212–221.

4 H. Ali, E. Khan and I. Ilahi, Environmental chemistry and ecotoxicology of hazardous heavy metals: environmental persistence, toxicity, and bioaccumulation, *J. Chem.*, 2019, **2019**, 6730305.

5 S. Dutta, S. Fajal and S. K. Ghosh, Heavy metal-based toxic oxo-pollutants sequestration by advanced functional porous materials for safe drinking water, *Acc. Chem. Res.*, 2024, **57**, 2546–2560.

6 J. A. Korak, R. Huggins and M. Arias-Paic, Regeneration of pilot-scale ion exchange columns for hexavalent chromium removal, *Water Res.*, 2017, **118**, 141–151.

7 A. N. Tiwari, K. Tapadia and C. Thakur, An enhanced method for the removal of methyl violet dye using magnetite nanoparticles as an adsorbent: Isotherm, kinetic and thermodynamic study, *Water Sci. Technol.*, 2022, **86**, 625–642.

8 H. Abyar, S. Namroodi, Z. Gharekhani and F. Hajimoradloo, Life cycle and efficiency assessment of fixed-bed bioreactor using recycled shredded plastics compared with conventional activated sludge bioreactor for dairy wastewater treatment, *J. Water Proc. Eng.*, 2024, **64**, 105676.

9 V. E. Pakade, N. T. Tavengwa and L. M. Madikizela, Recent advances in hexavalent chromium removal from aqueous solutions by adsorptive methods, *RSC Adv.*, 2019, **9**, 26142–26164.

10 Y. Wang, H. Jin, Q. Ma, K. Mo, H. Mao, A. Feldhoff, X. Cao, Y. Li, F. Pan and Z. Jiang, A MOF glass membrane for gas separation, *Angew. Chem.*, 2020, **132**, 4395–4399.

11 A. Abou-Elyazed, Y. Sun, A. El-Nahas and A. Yousif, A green approach for enhancing the hydrophobicity of UiO-66(Zr) catalysts for biodiesel production at 298 K, *RSC Adv.*, 2020, **10**, 41283–41295.

12 W. Fan, X. Wang, B. Xu, Y. Wang, D. Liu, M. Zhang, Y. Shang, F. Dai, L. Zhang and D. Sun, Amino-functionalized MOFs with high physicochemical stability for efficient gas storage/separation, dye adsorption and catalytic performance, *J. Mater. Chem. A*, 2018, **6**, 24486–24495.

13 Y. P. Wu, J. W. Tian, S. Liu, B. Li, J. Zhao, L. F. Ma, D. S. Li, Y. Q. Lan and X. Bu, Bi-Microporous metal–organic frameworks with cubane $[M_4(OH)_4]$ (M = Ni, Co) clusters and pore-space partition for electrocatalytic methanol oxidation reaction, *Angew. Chem., Int. Ed.*, 2019, **58**, 12185–12189.

14 A. S. Abou-Elyazed, E. A. Shaban, Y. Sun, A. M. El-Nahas and T. I. Kashar, Solvent-free synthesis and characterization of bimetallic UiO-66(Zr/Sn) heterogeneous catalyst for biodiesel production, *Ind. Eng. Chem. Res.*, 2023, **62**, 9211–9220.

15 M. S. Rezk, M. T. Abdel-Aal, I. E. T. El Sayed and A. S. Abou-Elyazed, Enhanced biodiesel production via copper-modified MIL-100(Fe): Synergistic catalysis and kinetic insights, *Mol. Catal.*, 2025, **585**, 115374.

16 G. Li, T. Wang, S. Zhou, J. Wang, H. Lv, M. Han, D. P. Singh, A. Kumar and J. Jin, New highly luminescent 3D Tb(III)-MOF as selective sensor for antibiotics, *Inorg. Chem. Commun.*, 2021, **130**, 108756.

17 A. Kondo, T. Suzuki, R. Kotani and K. Maeda, Liquid/vapor-induced reversible dynamic structural transformation of a three-dimensional Cu-based MOF to a one-dimensional MOF showing gate adsorption, *Dalton Trans.*, 2017, **46**, 6762–6768.

18 S. K. Ghosh, S. Fajal, S. Dutta, Y. D. More and S. Mukherjee, Post-synthetically modified metal–organic frameworks for sensing and capture of water pollutants, *Dalton Trans.*, 2021, **50**, 17832–17850.

19 Z. Zhang, X. Li, E. A. Shaban, J. Meng, S. Abdel-Azeim, T. I. Kashar and A. S. Abou-Elyazed, Enhanced DBT removal with eco-friendly synthesis of bimetallic UiO-66(Zr/Sn^{2+}) catalyst, *J. Environ. Chem. Eng.*, 2025, **13**, 115440.

20 Y. Zorlu, D. Erbahar, A. Çetinkaya, A. Bulut, T. S. Erkal, A. O. Yazaydin, J. Beckmann and G. Yücesan, A cobalt arylphosphonate MOF – superior stability, sorption and magnetism, *Chem. Commun.*, 2019, **55**, 3053–3056.

21 K. Suresh and A. J. Matzger, Enhanced drug delivery by dissolution of amorphous drug encapsulated in a water unstable metal–organic framework (MOF), *Angew. Chem., Int. Ed.*, 2019, **58**, 16790–16794.

22 Z. Zhang, W. Sang, L. Xie and Y. Dai, Metal-organic frameworks for multimodal bioimaging and synergistic cancer chemotherapy, *Coord. Chem. Rev.*, 2019, **399**, 213022.

23 H. Furukawa, K. E. Cordova, M. O'Keeffe and O. M. Yaghi, The chemistry and applications of metal-organic frameworks, *Science*, 2013, **341**, 1230444.

24 Q. Chen, L. Tian, M. Ruan, Y. Liu, C. Peng, W. Cui, W. Liang, S. Shan and T. Hu, HKUST-1/ZIF-67 nanocomposites as heterogeneous Cu–Co-bimetallic Fenton-like catalysts for efficient removal of methylene blue, *ACS Appl. Nano Mater.*, 2024, **7**, 2370–2381.

25 J. McCarron, B. Turner and L. N. McHugh, Hybrid Framework Materials: Next-Generation Engineering Materials, *Adv. Eng. Mater.*, 2025, 2402554.

26 M. K. Khan, M. Raza, M. Shahbaz, U. Farooq and M. U. Akram, Recent advancement in energy storage technologies and their applications, *J. Energy Storage*, 2024, **92**, 112112.

27 A. Preuß, S. Notz, E. Kovalski, M. Korb, T. Blaudeck, X. Hu, J. Schuster, D. Miesel, T. Rüffer and A. Hildebrandt, Ferrocenyl-Pyrenes, Ferrocenyl-9,10-Phenanthrenediones, and Ferrocenyl-9,10-Dimethoxyphenanthrenes: Charge-

Transfer Studies and SWCNT Functionalization, *Chem.–Eur. J.*, 2020, **26**, 2635–2652.

28 G. Flora, D. Gupta and A. Tiwari, Toxicity of lead: a review with recent updates, *Interdiscip. Toxicol.*, 2012, **5**, 47.

29 T. A. Sani, E. Mohammadpour, A. Mohammadi, T. Memariani, M. V. Yazdi, R. Rezaee, D. Calina, A. O. Docea, M. Goumenou and L. Etemad, Cytotoxic and apoptogenic properties of Dracocephalum kotschyi aerial part different fractions on Calu-6 and Mehr-80 lung cancer cell lines, *Farmacia*, 2017, **65**, 189–199.

30 R. Msalmi, S. Elleuch, B. Hamdi, W. Abd El-Fattah, N. B. Hamadi and H. Naïli, Organically tuned white-light emission from two zero-dimensional Cd-based hybrids, *RSC Adv.*, 2022, **12**, 10431–10442.

31 F. Ahmadijokani, A. Ghaffarkhah, H. Molavi, S. Dutta, Y. Lu, S. Wuttke, M. Kamkar, O. J. Rojas and M. Arjmand, COF and MOF hybrids: advanced materials for wastewater treatment, *Adv. Funct. Mater.*, 2024, **34**, 2305527.

32 J. Liu, J. T. Culp, S. Natesakhawat, B. C. Bockrath, B. Zande, S. Sankar, G. Garberoglio and J. K. Johnson, Experimental and theoretical studies of gas adsorption in $Cu_3(BTC)_2$: an effective activation procedure, *J. Phys. Chem. C*, 2007, **111**, 9305–9313.

33 J. L. Rowsell and O. M. Yaghi, Effects of functionalization, catenation, and variation of the metal oxide and organic linking units on the low-pressure hydrogen adsorption properties of metal–organic frameworks, *J. Am. Chem. Soc.*, 2006, **128**, 1304–1315.

34 L. Zeng, H. Sun, T. Peng and T. Hui, Effect of glass content on sintering kinetics, microstructure and mechanical properties of glass-ceramics from coal fly ash and waste glass, *Mater. Chem. Phys.*, 2021, **260**, 124120.

35 J. H. Cavka, S. Jakobsen, U. Olsbye, N. Guillou, C. Lamberti, S. Bordiga and K. P. Lillerud, A new zirconium inorganic building brick forming metal organic frameworks with exceptional stability, *J. Am. Chem. Soc.*, 2008, **130**, 13850–13851.

36 A. S. Abou-Elyazed, A. I. Ftooh, Y. Sun, A. G. Ashry, A. K. Shaban, A. M. El-Nahas and A. M. Yousif, Solvent-free synthesis of HKUST-1 with abundant defect sites and its catalytic performance in the esterification reaction of oleic acid, *ACS Omega*, 2024, **9**, 37662–37671.

37 X. Meng, X. Xin, T. Zhang, Y. Yu and Y. Cheng, Preparation of millimeter-sized spherical SiO_2–Al_2O_3 with various acid catalysts for the acetalization of glycerol with acetone, *J. Porous Mater.*, 2024, **31**, 1015–1027.

38 K. Ramaiah, J. Prashanth, J. Haribabu, K. E. Srikanth, B. V. Reddy, R. Karvembu and K. L. Reddy, Vibrational spectroscopic (FT-IR, FT-Raman), anti-inflammatory, docking and molecular characteristic studies of Ni(II) complex of 2-aminonicotinaldehyde using theoretical and experimental methods, *J. Mol. Struct.*, 2019, **1175**, 769–781.

39 J. Fu, X. Liu, Y. Kong, R. Zhao, Y. Sun and A. S. Abou-Elyazed, Enhancing the Adsorption Performance of HKUST-1 by Adding NH_4F During Room-Temperature Synthesis for Desulfurization of Fuel Oil, *Energies*, 2025, **18**, 5344.

40 H. Zhou, Integrated adaptive systems based on stimuli responsive capsules, PhD thesis, University of Liverpool, 2023.

41 E.-R. Kenawy, E. A. Kamoun, Z. S. Ghaly, A.-b. M. Shokr, S. H. EL-Moslamy and A. S. Abou-Elyazed, Copper and fluorine-MOFs loaded-electrospun PVA/gelatin nanofibers for enhancing the antimicrobial activity of topical wound dressings: MOFs synthesis and spinning conditions optimization, *Mater. Chem. Phys.*, 2025, **332**, 130303.

42 N. C. Burtch, H. Jasuja and K. S. Walton, Water stability and adsorption in metal–organic frameworks, *Chem. Rev.*, 2014, **114**, 10575–10612.

43 T. Liu, X. Li, O. J. Curnow, J. Choi and A. C. Yip, Advancing zeolite design via ionic liquid templating approach, *CrystEngComm*, 2025, **200**.

44 Y. Liu, H. Wang, Y. Cui and N. Chen, Removal of copper ions from wastewater: a review, *Int. J. Environ. Res. Public Health*, 2023, **20**, 3885.

45 X. Chen, X. Peng, L. Jiang, X. Yuan, H. Yu, H. Wang, J. Zhang and Q. Xia, Recent advances in titanium metal–organic frameworks and their derived materials: Features, fabrication, and photocatalytic applications, *Chem. Eng. J.*, 2020, **395**, 125080.

46 P. K. Pandey, S. Sharma and S. Sambi, Removal of lead(II) from waste water on zeolite-NaX, *J. Environ. Chem. Eng.*, 2015, **3**, 2604–2610.

47 M. Şener, B. Kayan, S. Akay, B. Gözmen and D. Kalderis, Fe-modified sporopollenin as a composite biosorbent for the removal of Pb^{2+} from aqueous solutions, *Desalin. Water Treat.*, 2016, **57**, 28294–28312.

48 M. M. Montazer-Rahmati, P. Rabbani, A. Abdolali and A. R. Keshtkar, Kinetics and equilibrium studies on biosorption of cadmium, lead, and nickel ions from aqueous solutions by intact and chemically modified brown algae, *J. Hazard. Mater.*, 2011, **185**, 401–407.

49 A. S. Abdelmoaty, S. T. El-Wakeel, N. Fathy and A. A. Hanna, High performance of UiO-66 metal–organic framework modified with melamine for uptaking of lead and cadmium from aqueous solutions, *J. Inorg. Organomet. Polym. Mater.*, 2022, **32**, 2557–2567.

50 K. Obayomi and M. Auta, Development of microporous activated Aloji clay for adsorption of lead(II) ions from aqueous solution, *Heliyon*, 2019, **5**, e02799.

51 Y. Gu, Y. Wang, H. Li, W. Qin, H. Zhang, G. Wang, Y. Zhang and H. Zhao, Fabrication of hierarchically porous NH_2-MIL-53/wood-carbon hybrid membrane for highly effective and selective sequestration of Pb^{2+}, *Chem. Eng. J.*, 2020, **387**, 124141.

52 H. Zhu, J. Yuan, X. Tan, W. Zhang, M. Fang and X. Wang, Efficient removal of Pb^{2+} by Tb-MOFs: identifying the adsorption mechanism through experimental and theoretical investigations, *Environ. Sci.: Nano*, 2019, **6**, 261–272.

53 K. Y. Foo and B. H. Hameed, Insights into the modeling of adsorption isotherm systems, *Chem. Eng. J.*, 2010, **156**, 2–10.

54 R. Ezzati, A new insight into the pseudo-second-order model and the physical meaning of its rate constant in adsorption, *J. Dispersion Sci. Technol.*, 2025, **46**, 222–229.

55 V. Kumar, Adsorption kinetics and isotherms for the removal of rhodamine B dye and Pb^{+2} ions from aqueous solutions by a hybrid ion-exchanger, *Arabian J. Chem.*, 2019, **12**, 316–329.

56 J. Wang and X. Guo, Adsorption isotherm models: Classification, physical meaning, application and solving method, *Chemosphere*, 2020, **258**, 127279.

57 J.-W. Fan, H.-D. Huang, H.-Y. Liu, B. Su and Z.-Y. Guo, Nanofiber films reinforced with biomass extracts and their high efficiency in adsorbing dyes, *Chem. Phys. Lett.*, 2024, **849**, 141394.

58 L. Lu, L. Li, M. Chu, C. Chen, B. Wang, J. Wang, Y. Shen, R. Ma, B. Li and L. Shen, Recent Advancement in 2D Metal–Organic Framework for Environmental Remediation: A Review, *Adv. Funct. Mater.*, 2025, **35**, 2419433.

59 K. K. Hammud, Isothermal adsorption models: mini-focused observations, *J. Pet. Res. Stud.*, 2023, **13**, 132–145.

60 M. A. Al-Ghouti and D. A. Da'ana, Guidelines for the use and interpretation of adsorption isotherm models: A review, *J. Hazard. Mater.*, 2020, **393**, 122383.

61 F. K. Mostafapour, A. H. Mahvi, A. D. Khatibi, M. K. Saloot, N. Mohammadzadeh and D. Balarak, Adsorption of lead(II) using bioadsorbent prepared from immobilized Gracilaria corticata algae: thermodynamics, kinetics and isotherm analysis, *Desalin. Water Treat.*, 2022, **265**, 103–113.

62 M. Yusuf, I. Kurzina, G. Voronova, M. Mohamed, S. D. Mohammed and N. A. Oladoja, Trends in the Energy and Environmental Application of Metal-Organic Framework-Based Materials, *Energy Adv.*, 2024, 2079–2135.

63 Z. Zhang, S. He, Y. Zhang, K. Zhang, J. Wang, R. Jing, X. Yang, Z. Hu, X. Lin and Y. Li, Spectroscopic investigation of Cu^{2+}, Pb^{2+} and Cd^{2+} adsorption behaviors by chitosan-coated argillaceous limestone: Competition and mechanisms, *Environ. Pollut.*, 2019, **254**, 112938.

64 W. Shenjin, L. Xiaoxi, Z. Chenyang, H. Wenjihao, L. Yaochi, F. Xinzhuang, Y. Jun and S. Wei, Adsorption and selective mechanism of Pb^{2+} and Cd^{2+} on the surface of calcined modified attapulgite, *Sep. Purif. Technol.*, 2025, **353**, 128377.

65 M. Y. Nassar, I. S. Ahmed, T. Y. Mohamed and M. Khatab, A controlled, template-free, and hydrothermal synthesis route to sphere-like α-Fe_2O_3 nanostructures for textile dye removal, *RSC Adv.*, 2016, **6**, 20001–20013.

66 H. N. Tran, S.-J. You, A. Hosseini-Bandegharaei and H.-P. Chao, Mistakes and inconsistencies regarding adsorption of contaminants from aqueous solutions: A critical review, *Water Res.*, 2017, **120**, 88–116.

67 R. Niwas, U. Gupta, A. A. Khan and K. G. Varshney, The adsorption of phosphamidon on the surface of styrene supported zirconium(IV) tungstophosphate: a thermodynamic study, *Colloids Surf., A*, 2000, **164**, 115–119.

68 A. A. Khan and R. P. Singh, Adsorption thermodynamics of carbofuran on Sn(IV) arsenosilicate in H^+, Na^+ and Ca^{2+} forms, *Colloids Surf.*, 1987, **24**, 33–42.

69 M. Y. Nassar, E. I. Ali and E. S. Zakaria, Tunable auto-combustion preparation of TiO_2 nanostructures as efficient adsorbents for the removal of an anionic textile dye, *RSC Adv.*, 2017, **7**, 8034–8050.